J. Fluid Mech. (2001), *vol.* 439, *pp.* 305–333. Printed in the United Kingdom

Large-eddy simulation of boundary-layer separation and transition at a change of surface curvature

By ZHIYIN YANG[1] AND PETER R. VOKE[2]

[1]Department of Aeronautical and Automotive Engineering, Loughborough University, Loughborough LE11 3TU, UK

[2] School of Mechanical and Materials Engineering, University of Surrey, Guildford GU2 5XH, UK

(Received 4 January 2000 and in revised form 28 September 2000)

Transition arising from a separated region of flow is quite common and plays an important role in engineering. It is difficult to predict using conventional models and the transition mechanism is still not fully understood. We report the results of a numerical simulation to study the physics of separated boundary-layer transition induced by a change of curvature of the surface. The geometry is a flat plate with a semicircular leading edge. The Reynolds number based on the uniform inlet velocity and the leading-edge diameter is 3450. The simulated mean and turbulence quantities compare well with the available experimental data.

The numerical data have been comprehensively analysed to elucidate the entire transition process leading to breakdown to turbulence. It is evident from the simulation that the primary two-dimensional instability originates from the free shear in the bubble as the free shear layer is inviscidly unstable via the Kelvin–Helmholtz mechanism. These initial two-dimensional instability waves grow downstream with a amplification rate usually larger than that of Tollmien–Schlichting waves. Three-dimensional motions start to develop slowly under any small spanwise disturbance via a secondary instability mechanism associated with distortion of two-dimensional spanwise vortices and the formation of a spanwise peak–valley wave structure. Further downstream the distorted spanwise two-dimensional vortices roll up, leading to streamwise vorticity formation. Significant growth of three-dimensional motions occurs at about half the mean bubble length with hairpin vortices appearing at this stage, leading eventually to full breakdown to turbulence around the mean reattachment point. Vortex shedding from the separated shear layer is also observed and the 'instantaneous reattachment' position moves over a distance up to 50% of the mean reattachment length. Following reattachment, a turbulent boundary layer is established very quickly, but it is different from an equilibrium boundary layer.

1. Introduction

Although boundary-layer separation and transition occur in many engineering flows of great practical importance, and understanding of the transition mechanisms and the unsteady structures is still increasing, our ability to predict and control it is still far from complete.

A free shear layer is formed as a laminar boundary layer separates owing to curvature changes or an adverse pressure gradient. When the boundary layer separates,

the free shear layer formed in the separation bubble is inviscidly unstable; the instability at work could be the Kelvin–Helmholtz mechanism, similar to that in the mixing layer and jet (Ho & Huerre 1984; Danaila, Dusek & Anselmet 1997; Urbin & Metais 1997). Generally, the amplification is larger in the case of an inviscid instability than is the case for viscous instabilities (Tollmien–Schlichting waves) (Schlichting 1968; Ho & Huerre 1984). It has been shown theoretically and experimentally by Gaster (1963) and more recently by Dovgal, Kozlov & Michalke (1994) that the laminar part of the bubble is indeed acting as a spatial filter-amplifier of upstream disturbances. It is believed that transition takes place owing to nonlinear breakdown of spatially growing travelling waves in the separated free shear layer. Dovgal *et al.* (1994) presents many results from theoretical (linear instability theory) and experimental studies of instability and other transitional phenomena in pre-separated and separated flows. Strong growth of the disturbances in the bubble is expected, as argued by Dovgal *et al.* (1994), since local velocity profiles with an inflection point exist. Such profiles are inviscidly unstable. However, the experimental data and theoretical results cited in Dovgal *et al.* (1994) on the nonlinear stage, especially breakdown to turbulence, are very limited and some aspects such as the large-scale structures in the bubble, and the highly unsteady flow behaviour around the mean reattachment region are not covered.

A flow is termed convectively unstable if the disturbances grow in space, convecting away from the source, whereas it is called absolutely unstable if the disturbances grow in time and spread everywhere. The possible existence of regions of absolute instability in separation bubbles was first raised by Gaster (1963). Niew (1993), by carrying out a linear wave packet analysis, showed that velocity profiles with strong reverse flow and high enough Reynolds number exhibit the characteristics of absolute instability. This was confirmed in a laminar separation bubble created by suction of fluid through the upper boundary in the simulation by Alam & Sandham (1999), who analysed their direct numerical simulation (DNS) data using Niew's method. They demonstrated that velocity profiles with strong reverse flow (more than 15%) exhibit characteristics of absolute instability. DNS by Rist, Maucher & Wagner (1996) indicates strongly that thin laminar separation bubbles are convectively unstable to short-wavelength disturbances of small amplitude initiated upstream of the bubble.

Pauley, Moin & Reynolds (1990) studied numerically a two-dimensional separation bubble created on a flat plate by a strong adverse pressure gradient and observed vortex shedding with a dimensionless shedding frequency (Strouhal number) of about 0.007. They also demonstrated that the vortices are indeed formed as a result of an inviscid instability of the detached shear layer in the separation bubble, and the shedding frequency is consistent with linear stability analysis. Several articles have also reported numerical simulations of a transitional separation bubble (Lin & Pauley 1993*a*, *b*; Ripley & Pauley 1993; Wilson & Pauley 1995) and the results compare well with experimental data even though the simulations were all two-dimensional. Recently, DNS of a transitional separation bubble on a flat surface due to aspiration through an opposite boundary by Spalart & Strelets (2000) suggests that the Kelvin–Helmholtz instability is involved.

Many experimental studies have been carried out on high-Reynolds-number separation/reattachment flow where the separation bubble is formed at a sharp corner, for instance at the leading edge of a blunt plate with right-angled corners. The time-mean velocity, pressure, turbulence intensity and Reynolds shear stress in such a separation bubble are reported by several workers (Ota & Itasaka 1976: Ota & Narita 1978; Kiya, Sasaki & Arte 1982). Measurements have also been made of the power spec-

trum, the integral timescale, the cross-correlation between the surface-pressure and velocity fluctuations, the reverse-flow intermittency and the phase velocities of fluctuations (Hillier & Cherry 1981*a*, *b*; Kiya & Sasaki, 1983; Cherry, Hillier & Latour 1984). The structure of the large-scale vortices in the turbulent separation bubble and the unsteady reverse flow in the reattachment zone were studied by Kiya & Sasaki (1985) using conditional-sampling techniques, and also by Cherry *et al.* (1984) with instantaneous smoke-flow visualization. Kiya & Sasaki (1985) inspected their space–time vector fields carefully and interpreted the structures observed as hairpin vortices.

DNS of a separated turbulent boundary layer on a flat plate in an adverse pressure gradient has been carried out recently by Na & Moin (1998). Their results show that large-scale structures grow in the shear layer and agglomerate, impinging on the wall and subsequently convecting downstream. The characteristic Strouhal number based on the inlet displacement thickness deduced from the movement of the spanwise-averaged reattachment point in their study ranges between 0.0025 and 0.01. Gartshore & Savill (1982) have reported the irregular formation of large structures downstream of reattachment for a normal flat-plate/splitter-plate combination, and have suggested that the instantaneous reattachment position moves over a distance of up to 50% of the time-averaged reattachment length. A similar observation was made by Eaton & Johnston (1981) for the flow over a backward-facing step.

The average frequency of vortex shedding measured by several workers (Kiya & Sasaki 1983, 1985; Cherry *et al.* 1984) is about $0.6–0.7U_0/l$, where U_0 is the free-stream velocity and l is the time-averaged bubble length. Hillier & Cherry (1981*a*) first showed the existence of a low-frequency ($0.12–0.2U_0/l$) unsteadiness in the separation bubble which was later confirmed by Kiya & Sasaki (1983, 1985) and Cherry *et al.* (1984). This low-frequency flapping of the separated shear layer was also observed in the separation bubble behind a backward-facing step by Eaton & Johnston (1982). The low-frequency flapping is not fully understood, but Eaton & Johnston (1982) suggest that the likely cause of the motion is an instantaneous imbalance between the entrainment rate from the recirculation zone and the reinjection near the reattachment line. Tafti & Vanka (1991) have carried out three-dimensional numerical simulation of the unsteady separated flow over a blunt plate held normal to a uniform stream. Their results compare reasonably well with the experimental data of Kiya & Sasaki (1983) and Cherry *et al.* (1984) despite the Reynolds number in their simulation being much lower. Their calculation also captured the experimentally observed low-frequency unsteadiness of the separation bubble. In addition, a selective high-frequency shedding from the separated shear layer was present in their numerical results.

The present study employs large-eddy simulation to investigate separated boundary-layer transition where the separation bubble is induced by a change of curvature of the surface on a flat plate with a semicircular leading edge. Separated laminar boundary-layer transition to turbulence is a very complex and many-sided problem which is still far from being completely understood despite the information obtained from the studies of separation and reattachment mentioned above, in which the separation is induced differently from the present study. In particular, the information obtained so far is not adequate for clarifying the entire transition process, large-scale structures and the instability mechanisms. Hence, the objectives of this paper are:

(i) To elucidate the complete transition process from laminar separation to reattachment and further downstream to turbulent boundary-layer flow, when separation is produced on a flat plate owing to a surface curvature change. In particular, to identify the primary instability mechanism, to check if absolute instability exists locally in the separation bubble and to show the process of nonlinear breakdown to turbu-

lence and the subsequent development beyond reattachment, comparing turbulence statistics with available experimental data.

(ii) To further clarify and identify the existence of any large-scale structures at different stages in the transition process. In particular, to verify the existence of hairpin vortices postulated by Kiya & Sasaki (1985) based on their experimental results.

(iii) To quantify the unsteady movement of the instantaneous reattachment point, and comparing with Gartshore & Savill's (1982) suggestions that it can move over a distance of up to 50% of the mean reattachment length.

(iv) To check for the existence of vortex shedding and, in particular, for the existence of low-frequency shear-layer flapping reported experimentally in the separation bubble formed on a blunt flat plate with right-angled corners (Hillier & Cherry 1981*a*; Kiya & Sasaki 1983, 1985; Cherry *et al.* 1984) and for the high selective frequency shedding reported numerically by Tafti & Vanka (1991).

2. Methods

Details of the mathematical formulation and numerical methods in general coordinates used in the present study have been reported elsewhere (Voke & Yang 1998, 1999) and are very similar to those implemented by Kaltenbach & Choi (1995). A brief description will be given below.

2.1. *Covariant Navier–Stokes equations*

The incompressible Navier–Stokes equations can be written in a form that is completely coordinate independent, or covariant:

$$\partial_t v^i = -\partial_j g^{ij} p/\rho + (-v^i v^j + 2\nu s^{ij})_{,j}, \tag{1}$$

where the strain rate is given by

$$s^{ij} = \tfrac{1}{2}(g^{ik} v^j_{,k} + g^{jk} v^i_{,k}), \tag{2}$$

g^{ij} is the metric tensor, and v^i is the contravariant component of velocity. The comma notation denotes covariant differentiation. We introduce J, the Jacobian of the transformation and

$$u^i = J v^i, \tag{3}$$

which is proportional to the mass flux across the coordinate lines rather than the contravariant velocities. The momentum equation becomes

$$\partial_t u^i = -J g^{ij} \partial_j p/\rho + \partial_j S^{ij} + \Gamma^i_{kj} S^{kj}, \tag{4}$$

$$S^{ij} = -u^i u^j/J + J\nu s^{ij}. \tag{5}$$

The Γ^i_{jk} are the connection coefficients or Christoffel symbols, derived from the metric tensor. The mass conservation equation is particularly simple using u variables, since

$$v^i_{,i} = \partial_i v^i + \Gamma^i_{ij} v^j = J^{-1} \partial_i (J v^i) = J^{-1} \partial_i u^i, \tag{6}$$

which gives

$$\partial_i u^i = 0. \tag{7}$$

In the simulations we use u^i as a variable except for computing s^{ij}, and the momentum advancement is explicit using the second-order Adams–Bashforth scheme except for the pressure term which is solved by a standard projection method. The pressure

equation is discrete Fourier transformed in z (a very rapid computational task) to obtain a set of decoupled equations that are solved by a multigrid technique with line relaxation acting as a smoother. The spatial discretization is second-order central differencing, with the geometric quantities computed to higher order in space in advance of the simulation and stored, as necessary, at several distinct points of a staggered mesh arrangement.

2.2. *Dynamic subgrid-scale model in general coordinates*

The finite-volume method with a staggered grid is used in the present study. The method was originally developed for large-eddy simulation (LES) by Deardorff (1970) and extended by Schumann (1973, 1975). The equations are integrated over control volumes, equivalent to a convolution with a tophat filter, and hence the velocity components at the corresponding grid points are the volume average. Any small-scale motions (smaller than the mesh or control volume) are averaged out and are accounted for by a subgrid-scale model. In the present study, a dynamic subgrid-scale model in general coordinates is used and described below.

The filtered Navier–Stokes equations in the transformed plane is:

$$\partial_t \overline{v^i} = -g^{ij}\partial_j \bar{p}/\rho + (-\overline{v^i v^j} + 2\nu \overline{s^{ij}})_{,j}. \tag{8}$$

The term $(\overline{v^i v^j})$ cannot be computed, and the difference between it and the part that can be computed $\overline{v^i}\,\overline{v^j}$ is the subgrid Reynolds stress τ^{ij}, analogous to the familiar Reynolds stress occurring in the time-average Navier–Stokes equations:

$$\tau^{ij} = (\overline{v^i v^j}) - \overline{v^i}\,\overline{v^j}. \tag{9}$$

The subgrid Reynolds stress represents the effects of the subgrid motions on the resolved fields of the LES. In contrast to the standard Reynolds stress whose length and velocity scales are those of the entire turbulent flow field, the lengthscale and velocity scale associated with the subgrid Reynolds stress can be deduced on a local basis from the mesh and the resolved velocity field of the simulation. If the length-scale is derived from the local mesh (Δ) and the velocity scale is dictated by the small-scale motions on the mesh, roughly equivalent to the largest subgrid velocities, based on the local strain rate scalar s, we obtain the Smagorinsky (1963) model. In general coordinates, it is as follows:

$$\tau^{ij} - g^{ij} g_{kl} \tau^{kl}/3 = -2\nu_s \overline{s^{ij}}, \tag{10}$$

$$\nu_s = C\Delta^2 \bar{s}, \tag{11}$$

$$\bar{s} = \sqrt{2 g_{ij} g_{kl} \overline{s^{ij}}\,\overline{s^{kl}}}. \tag{12}$$

C is predicted theoretically by Lilly (1966) to be 0.17^2.

This very simple model has been used widely and proved surprisingly successful, although it is possible that its longevity is partly due to our failure to find any better model for several decades. The model, in fact, has clear shortcomings. Tests of its predictions against directly simulated flow fields show that the correlation between the tensors in (10) is low. In shear flows, particularly wall-bounded flows, the model is too dissipative and the value of C has to be decreased to a much lower value. The reasons for this are now well understood, but this understanding has not led to a breakthrough to a special model for shear flows. Rather, it gave rise to a new approach in which the value of C, instead of being adjusted artificially based on the experience of the simulator, is deduced from the LES itself. The approach was

first proposed by Germano *et al.* (1991) and called a dynamic subgrid-scale model. It allows the value of C to respond to local flow conditions, varying in time and space.

A base subgrid-scale model such as Smagorinsky is needed first. We then consider what would happen if the same LES flow field were simulated on a coarser mesh, effectively filtering the velocity field with a filter larger than that actually used for the LES. This coarser filter, called the test filter, is usually chosen to be twice the size of the mesh filter. In general coordinates, we work in the transformed plane and take the filter to cover two cells rather than one. The test filter is represented by an overhat in the twice-filtered Navier–Stokes equations:

$$\partial_t \widehat{\overline{v^i}} = -g^{ij}\partial_j \widehat{\overline{p}}/\rho + (-\widehat{\overline{v^i v^j}} + 2\nu \widehat{\overline{s^{ij}}})_{,j}. \tag{13}$$

The subtest-scale stress is defined as

$$T^{ij} = (\widehat{\overline{v^i v^j}}) - \widehat{\overline{v^i}}\,\widehat{\overline{v^j}}. \tag{14}$$

We now apply the base (Smagorinsky) model at both filter scales, Δ and 2Δ:

$$\tau^{ij} - \tfrac{1}{3}g^{ij}g_{kl}\tau^{kl} = -2C\Delta^2 \overline{\bar{s}\,\overline{s^{ij}}}, \tag{15}$$

$$T^{ij} - \tfrac{1}{3}g^{ij}g_{kl}T^{kl} = -2C(2\Delta)^2 \widehat{\bar{s}}\,\widehat{\overline{s^{ij}}}. \tag{16}$$

Using the Germano identity, we obtain, in general coordinates,

$$l^{ij} = \widehat{\overline{v^i}\,\overline{v^j}} - \widehat{\overline{v^i}}\,\widehat{\overline{v^j}} = T^{ij} - \widehat{\tau^{ij}}, \tag{17}$$

$$L^{ij} = l^{ij} - \tfrac{1}{3}g^{ij}g_{kl}l^{kl} = T^{ij} - \tfrac{1}{3}g^{ij}g_{kl}T^{kl} - (\widehat{\tau^{ij}} - \tfrac{1}{3}g^{ij}g_{kl}\widehat{\tau^{kl}}) = -2CM^{ij}. \tag{18}$$

The models for T^{ij} and τ^{ij} are substituted to define the tensor M^{ij}:

$$M^{ij} = (2\Delta)^2 \widehat{\bar{s}}\,\widehat{\overline{s^{ij}}} - \Delta^2 \widehat{\overline{\bar{s}\,\overline{s^{ij}}}}, \tag{19}$$

thus,

$$C = -\frac{L^{ij}}{2M^{ij}}. \tag{20}$$

There are five separate equations for C since five components of each tensor on the right-hand side are independent, the tensors are symmetric and traceless as in the Cartesian case. The least-squares estimate of the optimal solution for C, following Lilly (1992), is

$$C = -\frac{\langle L^{ij}g_{ik}g_{jl}M^{kl}\rangle}{2\langle M^{ij}g_{ik}g_{jl}M^{kl}\rangle}. \tag{21}$$

The angle brackets represent an average over the homogeneous direction z in which C will not change. The resulting C is a function of time and the inhomogeneous coordinates x and y. This is a standard procedure in Cartesian coordinates and details can be found elsewhere (Germano *et al.* 1991; Lilly 1992). Ghosal *et al.* (1995) have proposed formulations which do not suffer the limitation that one direction must be statistically homogeneous.

The practical computation of C from equation (21) is considerably more complex than in the Cartesian case, owing to the presence of the metric tensor coupling the various components. An analogous derivation has been given for the generalized equations conserving the Cartesian components of momentum (Jordan 1999; Armenio, Piomelli & Fioretto 1999). A simple alternative that we have used for

the simulation whose results are given below is:

$$C = -\frac{\langle L^{ij} \rangle}{2\langle M^{ij} \rangle}, \tag{22}$$

selecting one of the five equations to define C. This is justified for the case considered in the next section where there is a clear principal strain rate and component of the subgrid Reynolds stress, such as the 12 component in a shear flow:

$$C = -\frac{\langle L^{12} \rangle}{2\langle M^{12} \rangle}. \tag{23}$$

A preliminary sensitivity study in the present case of transitional flow over a curved leading edge indicated that using the 12 component produced C values within 10% of the C values obtained from the least-squares methods using all six components whereas using other components such as 13 or 23 would produce very different C values. The final justification, however, is the considerable cost saving in using the dynamic procedure in this form, and the quality of the results.

Dynamic subgrid procedures have been applied successfully to a variety of flows in the past decade. Their popularity with simulators derives from the way they produce naturally the variation of C as solid walls are approached (making *ad hoc* damping functions such as the well-known Van Driest type unnecessary), the variation of C with Reynolds numbers (making LES of partially transitional flows a viable option) and the variation of C with flow type (for instance for stratified and other special flows). In the simulation of the transitional flow described below, the value of C increases from zero as the flow becomes unstable and reaches normal LES levels when the flow becomes fully turbulent. In fact, both M^{ij} and L^{ij} tend to zero in laminar regions, making equations (21) and (22) poorly conditioned or singular. This is not an academic point; the algorithm for computing C actually behaves unpredictably in laminar or nearly laminar regions and must be modified to ensure that C approaches zero in a sensible and well-defined manner. We do this by changing equation (23) (for the M^{12} component) to

$$C = -\frac{\langle L^{12} \rangle}{2(\langle M^{12} \rangle + \varepsilon)}, \tag{24}$$

where ε is a selected small quantity, related, for instance, to a global average of M^{12}. Typically, ε will be of the order of 10^{-5} of the values of M^{12} occurring in turbulent regions. It should be noted that in the present study the small value used for ε has no effect in the important flow region where M^{12} is much larger.

The subgrid-scale model is inactive in the laminar region before transition occurs and becomes active when significant growth of the disturbances starts in the separation bubble, with the largest values of ν_s/ν, occurring around the reattachment point being no greater than 8. The subgrid eddy viscosity reaches about 3 to 5 times the molecular viscosity at the end of the computational domain.

2.3. *Details of numerical computation*

The fully general coordinate system around this geometry is needed since an orthogonal coordinate system has an inconvenient junction between a cylindrical and a Cartesian mesh region at the critical point where the curved leading edge joins the flat surface. This is the point at which the laminar flow separates and starts to become unstable. Any disturbances in this region, including those with a numerical

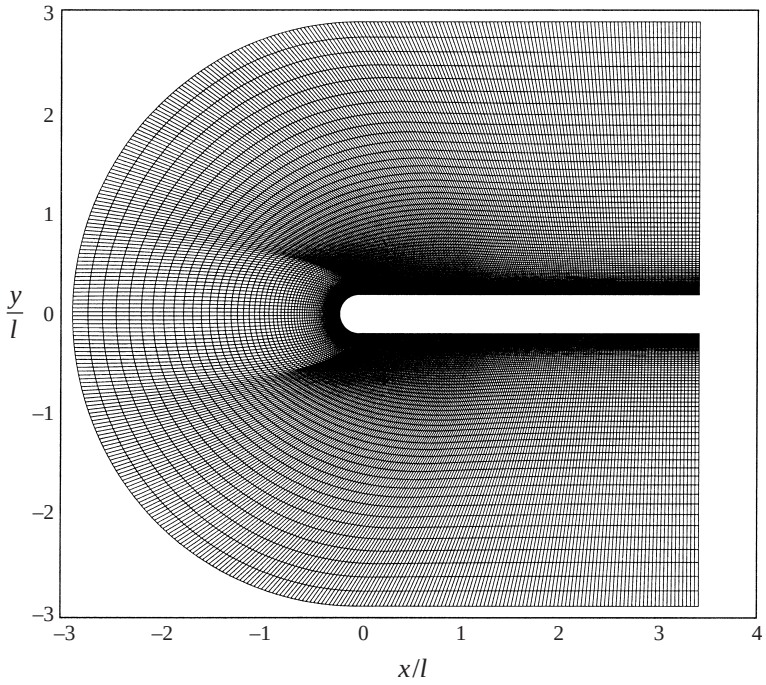

FIGURE 1. Computational domain and mesh.

origin, affect the flow and may lead to erroneous conclusions. A previous simulation (Voke, Yang & Savill 1996) used an orthogonal coordinate system and suffered from the problems indicated, including rapid and excessive growth of disturbances in the separated shear layer whose origin could be traced to numerical effects. This does not occur in the simulation with fully general curvilinear coordinates.

The overall geometry and meshing is shown in figure 1. The simulation uses 408 (streamwise, wrapped round the leading edge) by 72 (wall-normal, clustered in the near wall region) and there are about 10 grid points within the 99% boundary-layer thickness just before separation) by 64 (spanwise) meshes. The Reynolds number based on the plate leading-edge diameter d is 3450. The inflow velocity U_0 is uniform and aligned with the plate. The circular inflow boundary and the lateral boundaries are $8d$ distant from the surface, corresponding to a blockage ratio of 16. A free-slip but impermeable boundary is applied on the lateral boundaries. On the outflow boundaries, $9.5d$ downstream of the leading edge, a convective boundary condition is applied. The spanwise dimension of the domain is $2d$. Some simulations have been performed using a spanwise dimension of $4d$ without any appreciable change in the behaviour of the flow (less than 5% difference in terms of averaged statistics for both mean and turbulence stress).

In terms of wall units based on the shear layer downstream of reattachment at $x/l = 2.5$ (l is the mean separation bubble length), the streamwise mesh sizes vary from $\Delta x^+ = 10$ to 30.5, while $\Delta z^+ = 9$ and at the wall $\Delta y^+ = 1$ (the distance from the wall to the first cell location of u and w). The timestep used in the simulation is $0.005d/U_0$. The averaged subgrid eddy viscosity is about 3.5 times the molecular viscosity as the mesh resolutions are quite fine in most of the important flow regions and not far away from what would be recognized as DNS.

Statistics are gathered by averaging in time once the simulation is in its fully developed, statistically stationary state and also over the span direction and on both sides of the plate. The simulation is run for 40 000 timesteps to allow the transition and turbulent boundary layer to become established, and the results presented below are then gathered over a further 60 000 steps with a sample taken every 20 timesteps (3000 samples). Instantaneous flow fields and time traces of velocity components at certain points are also stored during the simulation for subsequent visualization and analysis.

3. Results and discussion

The simulation, like the experiment with which we compare it, has a low level of free-stream turbulence ($< 0.2\%$ in the experiment). In the simulation, pseudorandom body forcing is imposed at about $0.192l$ (l is the mean reattachment length) upstream of the blend point where the curvature changes (this is also the location of the x-axis origin where flow starts to separate) to mimic the low-turbulence level in the experiment. The amplitude of the forcing was initially selected to be 0.1% of the mean dynamic head ($0.5\rho U_0^2$) and was adjusted after some test runs to make sure that the turbulence level is about 0.1%. The simulation has also been performed with random disturbances imposed for only a very short time at the start; the transition process is found to be self-sustaining and the averaged results are very much the same as those presented here, with (at worst) less than 3% difference in significant quantities.

3.1. *Mean flow variables*

An important parameter characterizing a separated/reattached flow is the time mean position of the reattachment, i.e. time-averaged separation bubble length. The measured bubble length (J. Coupland, private communication 1994) is about $2.75d$ (d is the leading-edge diameter) and the simulated bubble length is about $2.6d$ which is in close agreement with the experimental data. The small difference is consistent with the difference in blockage ratio in the simulation (16 : 1) and the experiment (34 : 1).

Figures 2(*a*) and 2(*b*) show the mean and r.m.s. fluctuating parts of the streamwise velocity compared with experiment (Coupland, private communication) at seven streamwise stations. The profiles are plotted as functions of y/l at corresponding values of x/l where l is the mean reattachment length. As can be seen from figure 2(*a*), excellent agreement between the experimental data and the simulated results has been obtained for the mean streamwise velocity profiles. Differences in the free stream arise entirely from the differences in the blockage ratio.

The agreement for the r.m.s. fluctuations, as shown in figure 2(*b*), is also good, except that the simulation shows higher peaks of u' occurring closer to the wall at two stations in the bubble, especially at $x/l = 0.66$ where the discrepancy between the peak values is about 25%, but lack of experimental data (taken with a single hot-wire probe) in the near wall region makes detailed comparisons difficult. After the reattachment, the agreement is much better.

Figures 2(*c*) and 2(*d*) show the r.m.s. values of the vertical and spanwise fluctuations, but unfortunately there are no corresponding measurements to compare with. It is clear from figures 2(*b*), 2(*c*) and 2(*d*) that maximum fluctuations occur just before the mean reattachment point, with maximum values for u', v' and w' of about 24%, 18% and 19%, respectively. This is also true for the shear stress $\overline{u'v'}$, as can be seen from figure 2(*e*). Further downstream, the turbulence intensity reduces and reaches a stable value of about 15%, a typical turbulent boundary-layer level. The maximum r.m.s. values at about the mean reattachment point may be attributed to the unsteady

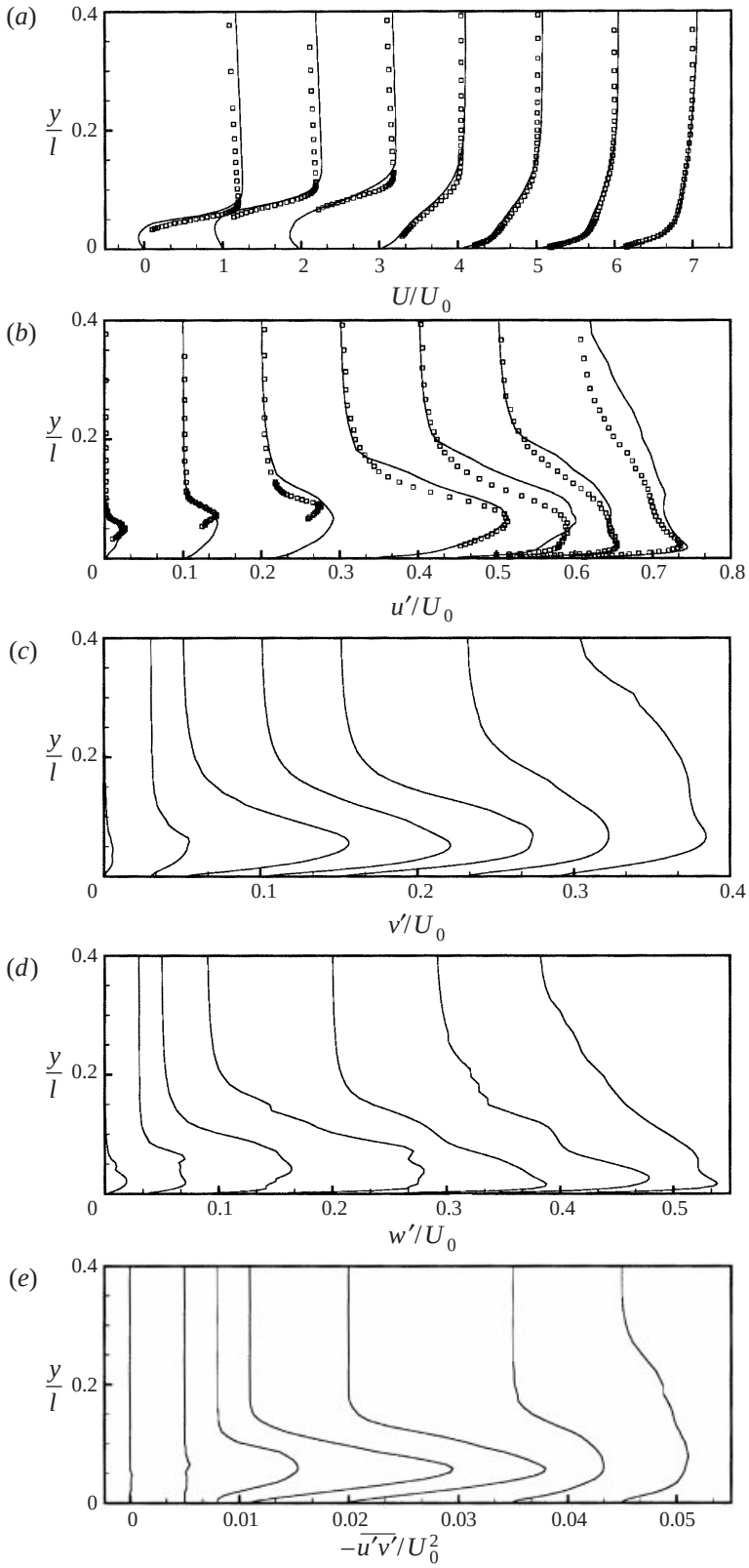

FIGURE 2. For caption see facing page.

large-scale movements and break-up in this region; these will be further explored in the following sections.

3.2. *Transition mechanisms*

3.2.1. *Description of the transition process*

The boundary layers develop in the densely meshed regions on either side of the plate, and are fully turbulent well before they reach the two outflow boundaries. The layers on either side of the plate are not symmetric and can be quite different instantaneously, just as they would be in reality (the time average flow field is symmetric on the two sides of the plate, but the instantaneous flow field may not be). The transition process can be clearly seen in figure 3 which shows the instantaneous spanwise vorticity at various times in the (x, y)-plane at an arbitrary z-(spanwise) plane. In the first half of the bubble a free shear layer develops and spanwise vortices forms; these are inviscidly unstable and any small disturbances present grow downstream with an amplification rate larger than that in the case of viscous instabilities. Further downstream, the initial spanwise vortices are distorted severely and deform, leading to streamwise vorticity formation associated with significant three-dimensional motions, eventually breaking down at about the reattachment point and developing rapidly into a turbulent boundary layer.

3.2.2. *Position of initial unsteadiness*

The flow is laminar and two-dimensional before the separation and even in some regions just after the separation, as can be seen from figure 4 which shows the instantaneous values of the three velocity components at three arbitrary times in a spanwise plane along the streamwise direction, starting from the blend point where the separation occurs. It can be seen clearly that the profiles at three different times are virtually the same when $x/l < 0.15$, with a zero value for the W velocity at different y-values, indicating that the flow is two-dimensional and steady. The profiles indicate that the initial unsteadiness occurs at about $x/l = 0.15$. The instantaneous spanwise velocity starts to develop slowly when $x/l > 0.15$ and remains small until $x/l = 0.5$, when significant three-dimensional motions start to develop very quickly and violently, with maximum values reaching almost 40% of the streamwise velocity in the free stream.

The profiles for the U and V velocity components show the same kind of pattern, with the initial unsteady motions observed to develop slowly and starting to develop very rapidly and violently at about $x/l = 0.5$. This may indicate that in the region from $x/l = 0.15$ up to $x/l = 0.5$ the disturbances grow linearly, with nonlinear rapid growth and breakdown starting from the region $x/l = 0.5$ onward.

The first appearance of unsteadiness can be further confirmed by looking at figures 5(*a*) to 5(*c*) which show the instantaneous streamwise velocity profile in a single spanwise plane at three streamwise locations and at three different times. The discrepancy between velocity profiles at three different times can barely be observed at $x/l = 0.2$ in figure 5(*a*) as the difference between the velocity at different times is still very small compared with the velocity itself (although figure 4 does indicate that the initial unsteadiness occurs in the region between $x/l = 0.15$ and

FIGURE 2. (*a*) Mean axial velocity, (*b*) r.m.s. streamwise velocity fluctuation u', (*c*) r.m.s. vertical velocity fluctuation v', (*d*) r.m.s. spanwise velocity fluctuation w' and (*e*) r.m.s. profiles of shear stress, measured at seven streamwise positions measured from the blend point. Left to right, $x/l = 0.22$, 0.44, 0.66, 1.09, 1.27, 1.64, 2.55. ——, LES; □ experimental data.

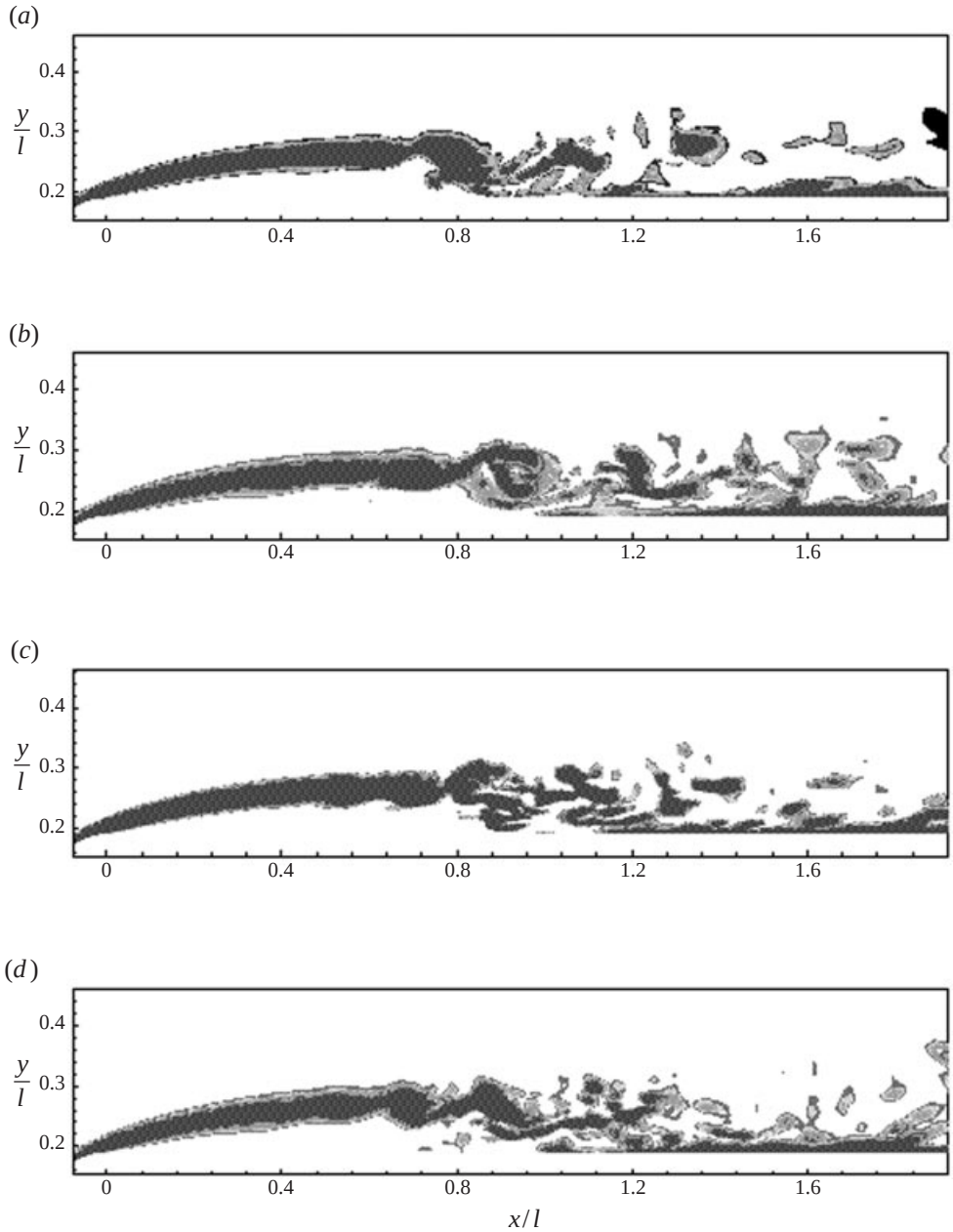

FIGURE 3. Instantaneous spanwise vorticity in the (x, y)-plane.

$x/l = 0.2$). The discrepancy between the instantaneous profiles grows downstream and becomes clearly apparent at $x/l = 0.4$, as shown in figure 5(b). Further downstream at $x/l = 0.8$, as shown in figure 5(c), the profiles are very distorted owing to very unsteady large-scale motions inducing violent fluctuations.

The growth of disturbances can be seen in figure 6, showing the peak r.m.s. values of the three velocity components along the x-coordinate starting from the blend point where the separation occurs. The r.m.s. values are almost zero at separation

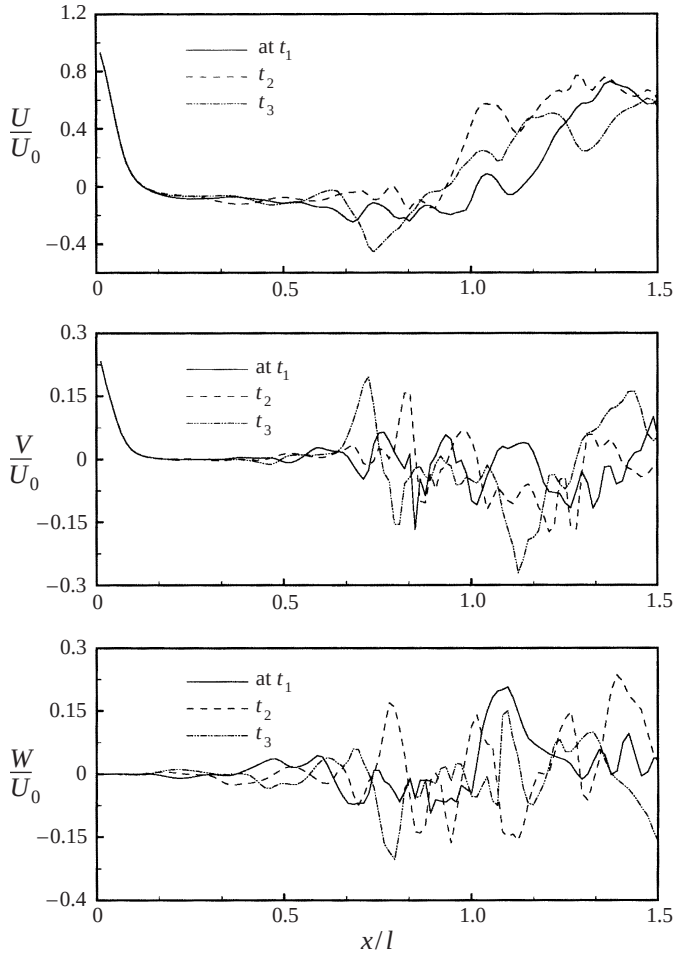

FIGURE 4. Instantaneous velocity profiles at $y/l = 0.015$.

and start to grow slowly in the first half of the bubble, with the peak r.m.s. values of u' and w' reaching only about 1.5% at 25% bubble length. The peak r.m.s. value of v' increases more slowly up to 1.5% at about half of the bubble length. However, the fluctuations increase very rapidly in the second half of the bubble, with w' and v' lagging behind u' slightly, reaching a maximum value just before the mean reattachment point, indicating that three-dimensional motion and nonlinear interaction lead to breakdown to turbulence in the second half of the bubble, from $x/l = 0.5$ to $x/l = 1.0$.

It is evident from the figures discussed above that the flow starts to become unsteady in the region from $x/l = 0.1$ to $x/l = 0.2$ and significant growth of the disturbances starts at about $x/l = 0.5$.

3.2.3. *Vortex shedding and movement of instantaneous reattachment*

A reattachment point or line in a steady laminar separation bubble can be defined as the position where the skin friction coefficient is zero. For the current transitional separated boundary-layer flow, the time average is similar to a steady laminar separated flow, but with a different bubble shape and separation length. This can be seen from figure 7(*a*), which shows clearly one separation bubble starting from the

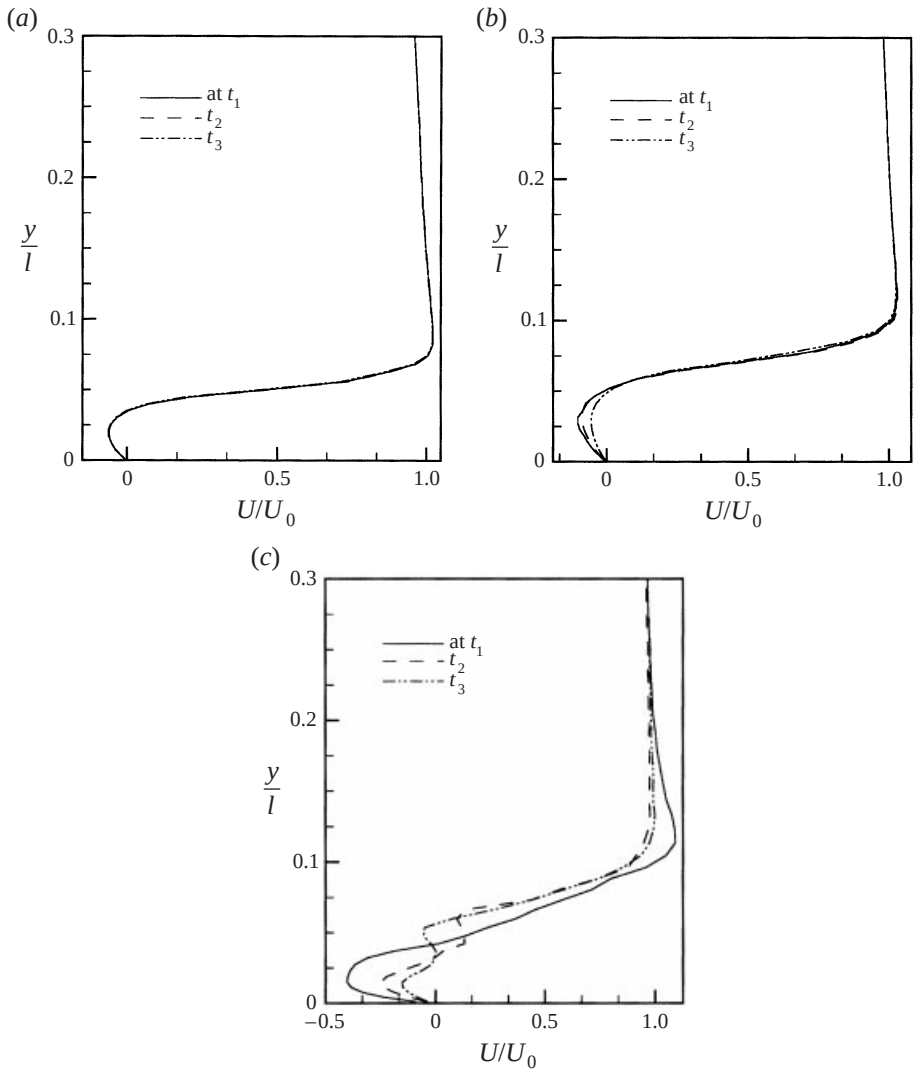

FIGURE 5. Instantaneous streamwise velocity profiles at (*a*) $x/l = 0.2$, (*b*) 0.4, (*c*) 0.8.

blend point with a smooth flow field, reattaching at about 2.6*d*. However, this is not representative of the instantaneous flow field as the flow becomes highly unsteady around the mean reattachment point. There can be several small bubbles or vortices formed, and vortex shedding may occur. We can confirm from figures 7(*b*), 7(*c*) and 7(*d*), showing instantaneous flow fields in the (x, y)-plane, that the instantaneous reattachment point is indeed highly variable with time. The instantaneous velocity vectors in an (x, y)-plane presented by Tafti & Vanka (1991) also show very similar flow features. Vortices, formed in the separated free shear layer owing to inviscid linear instability, shed downstream, agglomerate and impinge on the wall, collapse and lead to the breakdown to turbulence.

The unsteady movement of the instantaneous reattachment position and the irregular formation of large structures downstream of reattachment for a normal flat-plate/splitter-plate combination have been reported by Gartshore & Savill (1982).

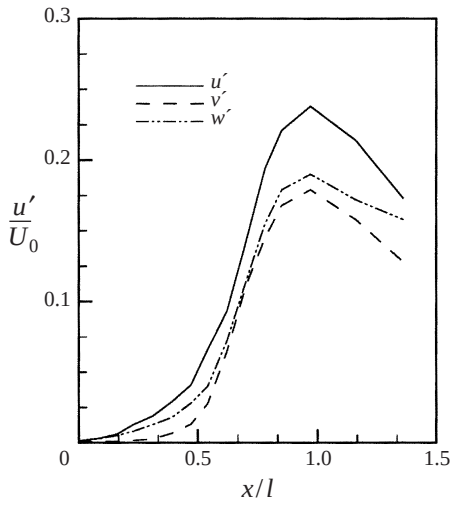

FIGURE 6. Profiles of maximum r.m.s. values.

A similar observation was made by Eaton & Johnston (1981) for the flow over a backward-facing step. Gartshore & Savill (1982) suggested that the position moves over a distance of up to 50% of the time-averaged reattachment length. Quantitative information is given in figure 8, which shows the variation of the instantaneous bubble length normalized by the mean bubble length. It can be seen that the instantaneous bubble length (the last instantaneous reattachment) fluctuates greatly. The maximum value is about $1.26l$ and the minimum value is only about $0.73l$. $l_{max} - l_{min} = 0.53l$, which is 53% of the averaged bubble length.

The measured average shedding frequency is about 0.6–$0.7U_0/l$ (Kiya & Sasaki 1983, 1985; Cherry *et al.* 1984) as mentioned earlier. To further clarify the vortex shedding frequency in the present study, power spectra of spanwise-averaged u' at $y/l = 0.04$ and three streamwise locations at $x/l = 0.35$, 0.7 and 0.96 are shown in figures 9(*a*)–9(*c*). Vortex shedding is present at $x/l = 0.35$ and is not periodic with a single frequency. The shedding process seems to happen within a range of frequency of roughly $0.52U_0/l$–$1.14U_0/l$ (the Strouhal number, hereinafter referred to as St, is 0.005–0.011 based on the free-stream velocity and displacement thickness just before the separation). The averaged frequency can be estimated at about $0.82U_0/l$ ($St = 0.0079$). In addition, there is also a peak at lower frequency, $0.104U_0/l$ ($St = 0.001$), as shown in figure 9(*a*) at $x/l = 0.35$, which may correspond to the measured low-frequency flapping of the free shear layer (Hillier & Cherry 1981*a*; Kiya & Sasaki 1983, 1985; Cherry *et al.* 1984). The pictures are similar at $x/l = 0.7$ and 0.96 except that the low-frequency peak is not as apparent as at $x/l = 0.35$. The shedding frequency range seems to become slightly wider from $0.34U_0/l$ to $1.04U_0/l$ (St is 0.00327–0.01) and the average frequency is about $0.72U_0/l$ ($St = 0.0069$). The predicted dominant frequency, $0.72U_0/l$–$0.82U_0/l$ (St is 0.0069–0.0079), is slightly larger than the measured value of $0.6U_0/l$–$0.7U_0/l$, but acceptable considering the geometry is different between the experiments (blunt flat plate with right-angled corners) and the present simulation (flat plate with a semicircular leading edge). The DNS results of a separated turbulent boundary layer by Na & Moin (1998) show similar ranges of Strouhal number from 0.0025 to 0.01, based on the inlet displacement thickness. The DNS of backward-facing step flow by Le, Moin & Kim (1997) also

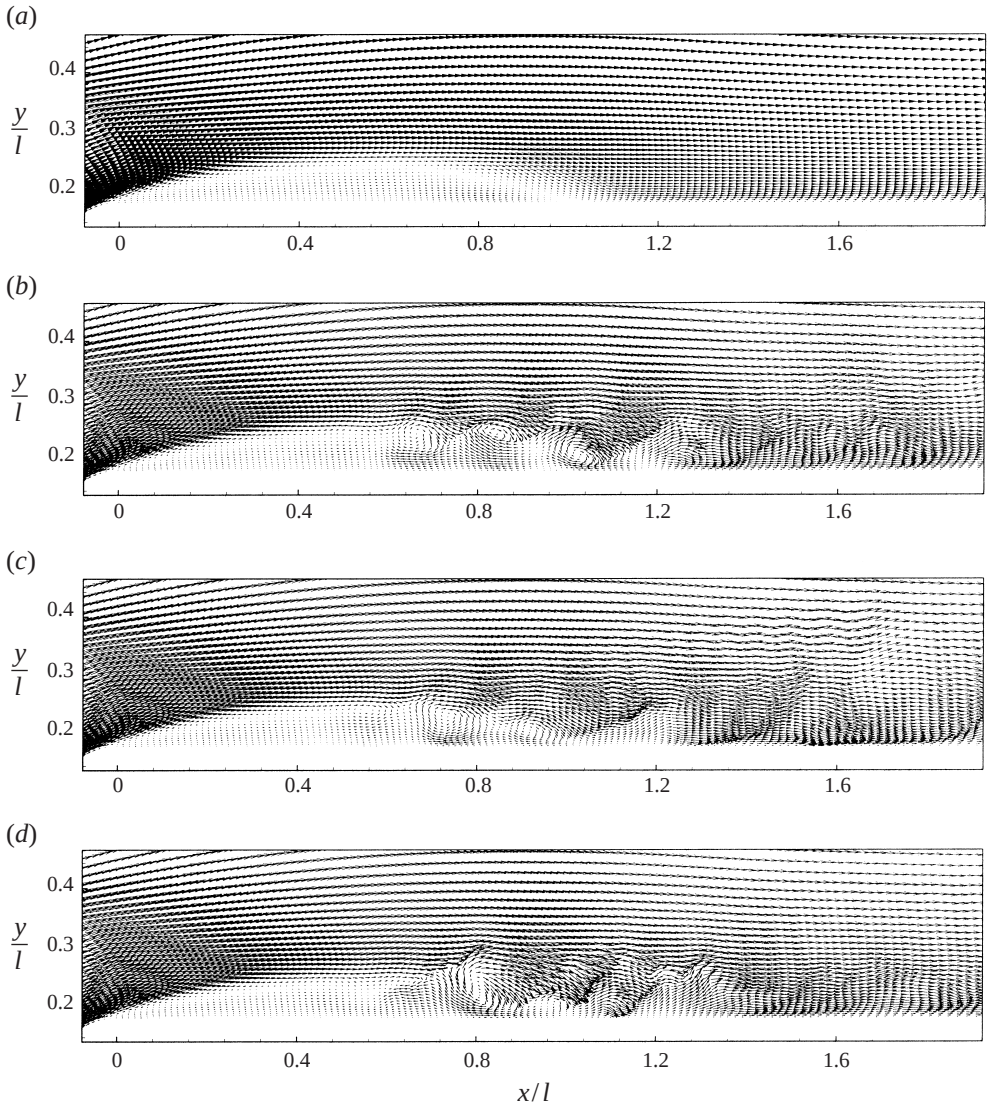

FIGURE 7. Velocity vectors (u, v) in the (x, y)-plane: (*a*) averaged results; (*b*)–(*d*) instantaneous results.

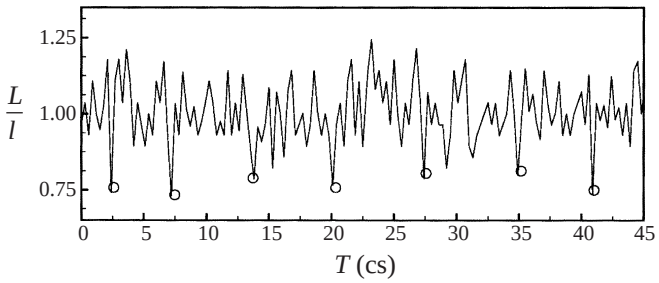

FIGURE 8. Variations of the instantaneous bubble length against time.

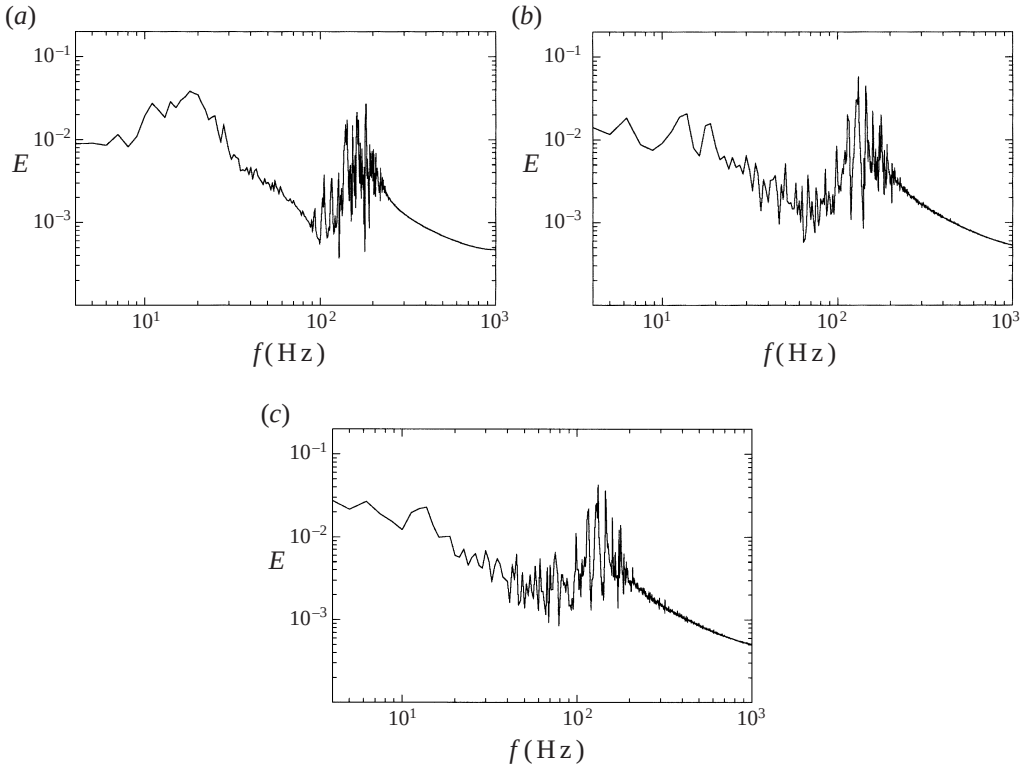

FIGURE 9. Power spectrum of u' at $y/l = 0.04$ and (*a*) $x/l = 0.35$, (*b*) 0.7, (*c*) 0.96.

shows that the Strouhal number corresponding to the dominant frequency is about 0.007 based on the inlet displacement thickness.

The so-called low-frequency flapping has been observed experimentally (Hillier & Cherry 1981*a*; Eaton & Johnston 1982; Kiya & Sasaki 1983, 1985; Cherry *et al.* 1984) and captured numerically (Tafti & Vanka 1991). However, the cause is still not fully understood. It is suggested by Eaton & Johnston (1982) that the probable cause of the motion is an instantaneous imbalance between the entrainment rate from the recirculation zone and the reinjection near the reattachment line. Tafti & Vanka (1991) postulate that it is caused by the periodic enlargement and shrinkage of the separation bubble. We think it is mainly due to another vortex-shedding phenomenon that occurs on a larger timescale in addition to the usual vortex shedding. On inspecting figures 7(*b*) and 7(*c*) carefully, it is seen that there can be several small bubbles formed inside or sitting on the tail of a big separation bubble. The vortex shedding we normally refer to is associated with the individual shedding of these small bubbles, which would not have a great impact on the big bubble, although the last instantaneous reattachment will change accordingly. However, it is possible that several small bubbles may occasionally form a larger one, or at some stage a relatively large bubble may form instead of several small ones, as indicated in figure 7(*d*). This relatively larger bubble collapses and sheds downstream, which will have a greater impact on the big bubble. The two topological structures of the separation bubble associated with the onset of vortex shedding are sketched in figure 10. The instantaneous reattachment length according to figure 10(*b*) must be shorter just after the shedding of the relatively big bubble compared with the case in

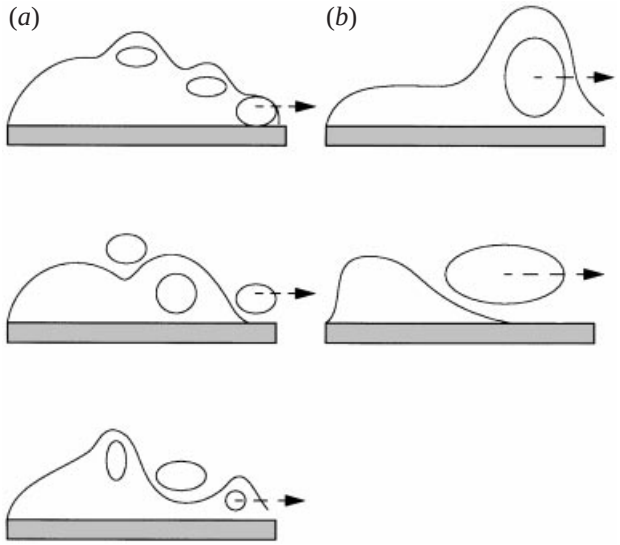

FIGURE 10. Two different topological structures of a separation bubble associated with the onset of vortex shedding: (*a*) normal shedding; (*b*) shedding responsible for the low-frequency flapping.

figure 10(*a*) and this can be confirmed in figure 8. It is evident that the instantaneous bubble length reduces to a much lower value from time to time, indicating that the bubble does shrink dramatically at times. The time interval between the lower peaks (indicated by circles) varies from 4.8 to 7.2, corresponding to a characteristic frequency from $0.072U_0/l$ to $0.108U_0/l$ (St from 0.0007 to 0.001), and the lower-frequency peak observed in figure 9 is indeed in this range.

3.2.4. *Primary instability mechanism*

It is well known that the necessary condition for a flow to be inviscidly unstable to small disturbances is that the velocity profile has an inflection point. This theorem was first formulated by Rayleigh (1880); later, Tollmien (1935) showed that the existence of an inflection point is also a sufficient condition for instability. The profiles shown in figures 5(*a*)–5(*c*) have an inflection point and hence are inviscidly unstable. To further clarify this, the present simulated results will be compared with inviscid linear stability analysis.

Consider a free shear layer between two streams, u_1 and u_2 which has, like a mixing layer, two distinct velocity scales: the velocity difference $\Delta u = u_2 - u_1$ and the average velocity $\bar{u} = \frac{1}{2}(u_1 + u_2)$. The free shear layer can be characterized by the vorticity thickness $\delta_w = \Delta u/(\mathrm{d}u/\mathrm{d}y)_{max}$ which defines a characteristic lengthscale and the velocity ratio $\lambda = \Delta u/(2\bar{u})$ which measures the magnitude of the velocity difference across the layer. When $\lambda = 0$, there is no shear. Monkewitz & Huerre (1982) have carried out inviscid analysis of parallel flow using the parallel tanh profile and found that the most amplified non-dimensional frequency, $\omega_{max} = (\frac{1}{4}\delta_w)(2\pi f/\bar{u})$, is not strongly dependent on either λ or the profile shape and changes only from 0.222 to 0.21 when λ varies from 0 to 1. In the unsteady region of free shear in the separation bubble, λ and the vorticity thickness change with streamwise distance and, hence, the non-dimensional shedding frequency ω_{max} varies. Pauley *et al.* (1990) computed from their two-dimensional simulation results that the non-dimensional frequency ω_{max} is indeed about 0.21 at the streamwise location of the centre of the

time-averaged separation bubble, where the new shed vortices are observed to form. In the present study, the most amplified non-dimensional frequency ω_{max} is calculated at several streamwise locations and the values change from 0.231 to 0.206. This close agreement between the simulated results and the inviscid linear stability analysis has been obtained for different values of λ, corresponding to several different streamwise locations, showing that the free shear layer in the bubble is unstable via an inviscid instability mechanism.

It is evident that the vortices are indeed formed as a result of the inviscid instability of the free shear layer, as the shedding frequency is consistent with the inviscid linear stability analysis. Kiya & Sasaki (1985) indicate from their separated boundary-layer study that the large-scale vortices originate from a successive amalgamation of vortices formed in the separated shear layer through the Kelvin–Helmholtz instability. In mixing-layer and jet-flow studies (Ho & Huerre 1984; Danaila *et al.* 1997; Urbin & Metais 1997) the mechanism is also believed to be the Kelvin–Helmholtz instability. However, sufficient and detailed evidence has not been given in these studies to show that the instability mechanism at work is indeed the Kelvin–Helmholtz instability. In order to clarify whether the instability of the free shear layer in the present study is the Kelvin–Helmholtzs instability, we consider the Kelvin–Helmholtz instability in more detail.

Let two uniform incompressible inviscid fluids of densities ρ_1 and ρ_2 and velocities U_1 and U_2 be separated by a horizontal boundary at $y = 0$. Let the density ρ_1 of the upper fluid be less than the density ρ_2 of the lower fluid so that the arrangement is a stable one when U_1 and U_2 are zero. For a given difference in velocity $U_2 - U_1$, no matter how small it is, instability occurs for all wave-numbers larger than a critical value (for disturbances of sufficiently small wavelengths) or it can be stated that, for a given wavenumber, instability occurs if the velocity difference $U_2 - U_1$ is larger than a critical value. This is the Kelvin–Helmholtz instability (Chandrasekhar 1961; Craik 1982). It may be said that the Kelvin–Helmholtz instability arises from the crinkling of the interface by the shear which is present, and this crinkling occurs even for the smallest difference in the velocity of the two fluids.

The question that must be answered is whether the Kelvin–Helmholtz instability is due to the sharp discontinuities in ρ and U which have been assumed in its derivation. Chandrasekhar (1961) considered the case of continuous variation of U and certain distribution of ρ (characterized by the Richardson number) and concluded from his inviscid linear stability analysis that, for any values of the Richardson number, there are always bands of wavelengths for which the Kelvin–Helmholtz instability occurs. In particular, when the Richardson number is zero, i.e. for constant density, the condition for the Kelvin–Helmholtz instability to occur is $0 < Kh < 1.2785$ where K is the wave number and h is the shear layer thickness. In the present study, the shear layer thickness at the region where the unsteadiness first becomes apparent (at about $x/l = 0.2$) is $0.0577l$, and hence the unstable region for K is $0 < K < 22.158/l$. In other words, the Kelvin–Helmholtz instability will not occur in the present study for wavenumbers larger than $22.158/l$, or wavelength smaller than $2\pi/K = 0.2836l$. From figure 9(*a*), the characteristic frequency varies from about $0.52U_0/l$ to $1.14U_0/l$ and the wave speed c is equal to the velocity at the critical layer, $U(Y_c)$, i.e. the streamwise velocity at the inflection point where $\mathrm{d}^2U(y_c)/\mathrm{d}y^2 = 0$, which is about $0.42U_0$ at $x/l = 0.2$. Therefore, the maximum wavenumber from the simulated results is $K_{max} = 2\pi f_{max}/c = 17.05/l$, corresponding to a wavelength of $0.368l$, which satisfies the Kelvin–Helmholtz instability criterion for the present study ($0 < K < 22.158/l$).

To check that this criterion is satisfied in the region between $x/l = 0.2$ and $x/l = 0.5$

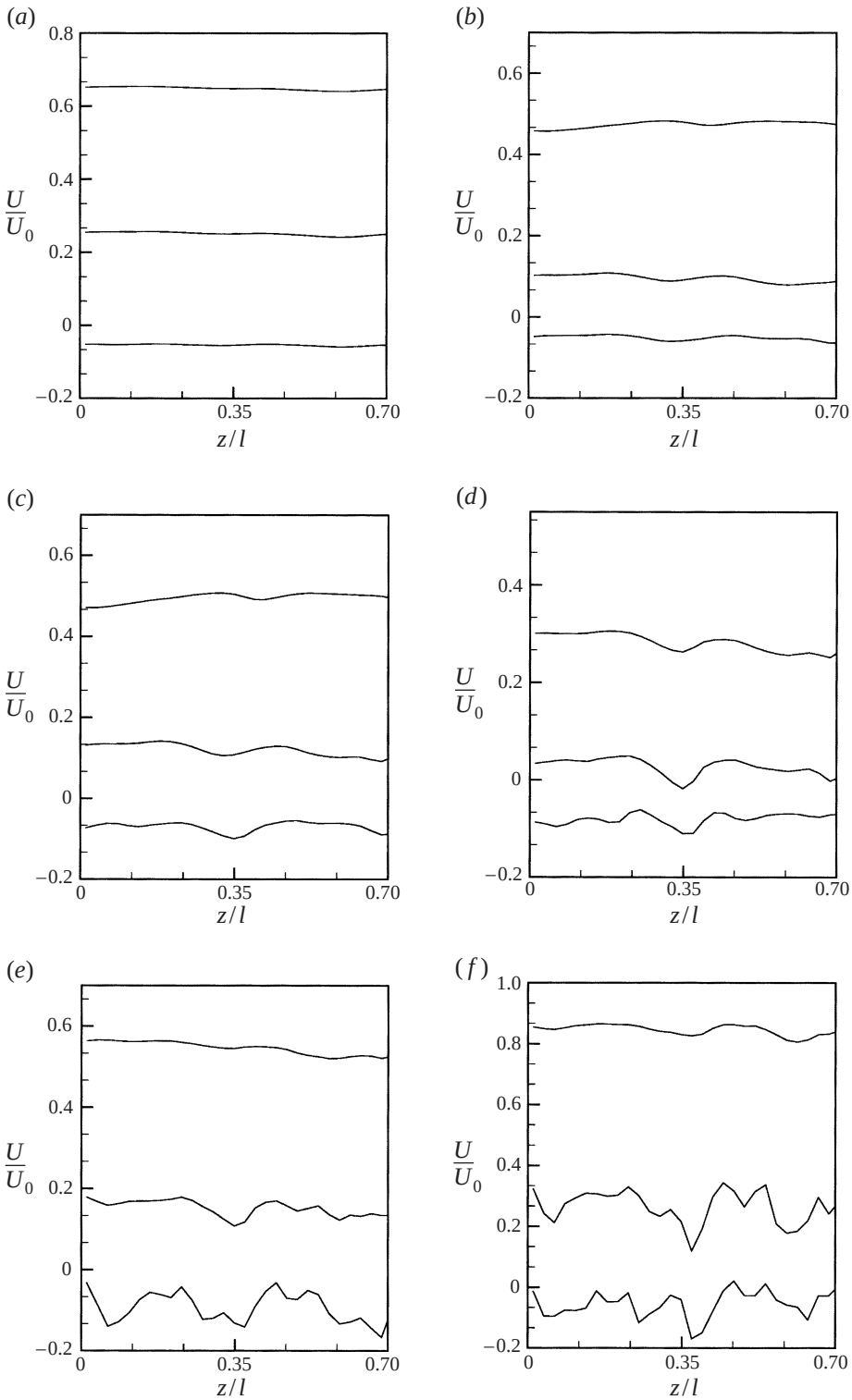

FIGURE 11. For caption see facing page

where the disturbance starts to grows significantly, let us consider another location, $x/l = 0.45$. The shear-layer thickness at $x/l = 0.45$ is about $0.073l$ and, hence, the unstable region for K is $0 < K < 17.5/l$. The wave speed at $x/l = 0.45$ is $0.584U_0$ and, hence, the maximum wavenumber is $k_{max} = 2\pi f_{max}/c = 12.3/l$ which indeed satisfies the Kelvin–Helmholtz instability criterion ($0 < K < 17.5/l$). Several locations in the range $0.2 < x/l < 0.45$ have also been checked and the maximum wavenumbers are all within the unstable region according to the Kelvin–Helmholtz instability criterion for constant density and continuous variation of U velocity (Chandrasekhar 1961). Thus, it can be concluded that the free shear layer in the separation bubble is likely to become inviscidly unstable via the Kelvin–Helmholtz instability mechanism.

The amount of reverse flow has also been calculated at several locations in the bubble to check if there exists an absolute instability region, as Alam & Sandham (1999) demonstrated that velocity profiles with strong reverse flow (more than 15%) exhibit the characteristics of absolute instability. It has been found that the maximum reverse flow in the present study is smaller than 3% and, hence, on the assumption that our bubble behaves similarly to Alam's there is no absolute instability region existing in the separation bubble.

3.2.5. *Development of three-dimensional motions, structures and breakdown to turbulence*

As shown in figure 6, significant growth of disturbances starts at about $x/l = 0.5$, u' and w' seem to develop soon after the separation point very slowly until $x/l = 0.2$ where u' starts to develop slightly more quickly. u' and w' are more or less of the same order of magnitude, while v' is an order of magnitude smaller and its growth also lags behind the other two when $x/l < 0.45$. Significant growth of all disturbances (u', v', w') starts at around and after $x/l = 0.45$.

Another way of monitoring the development of three-dimensional motions is to see how the instantaneous spanwise velocity develops. Figure 4 shows the instantaneous spanwise velocity component against x/l at $y/l = 0.015$. It can be seen clearly from these figures that the spanwise instantaneous velocity is almost zero when $x/l < 0.15$ and starts to develop very slowly to a small value, while significant three-dimensional motions start to develop rapidly only when $x/l > 0.5$. This can be further confirmed in figures 11(*a*)–11(*f*), showing the variations of the instantaneous streamwise velocity along the spanwise direction at six streamwise locations, $x/l = 0.1$, 0.2, 0.3, 0.4, 0.5 and 0.6. At $x/l = 0.1$, the streamwise velocity profile is almost flat at all the vertical heights, indicating that it is two-dimensional flow. Slight distortion can be observed at $x/l = 0.2$ and develops slowly until $x/l = 0.5$ when significant three-dimensional motions are observable. These develop rapidly afterwards, figure 11(*f*) at $x/l = 0.6$, indicating that a three-dimensional state is achieved well before the mean reattachment. It can be seen from these figures that a peak–valley wave structure is present; the peak and valley values of the velocity profile at different spanwise locations indicate the formation of longitudinal vortices. Peaks form when fluid with larger streamwise velocity is pushed down from the layer above, and valleys when the fluid with lower velocity is pushed up from the layer below.

More detailed qualitative information regarding the development of three-

FIGURE 11. Instantaneous streamwise velocity profiles at (*a*) $x/l = 0.1$; bottom to top, $y/l = 0.008$, 0.026, 0.04; (*b*) $x/l = 0.2$; bottom to top, $y/l = 0.008$, 0.035, 0.05; (*c*) $x/l = 0.3$; bottom to top, $y/l = 0.018$, 0.045, 0.06; (*d*) $x/l = 0.4$; bottom to top, $y/l = 0.022$, 0.045, 0.06; (*e*) $x/l = 0.5$; bottom to top, $y/l = 0.035$, 0.055, 0.067; (*f*) $x/l = 0.6$; bottom to top, $y/l = 0.035$, 0.06, 0.08.

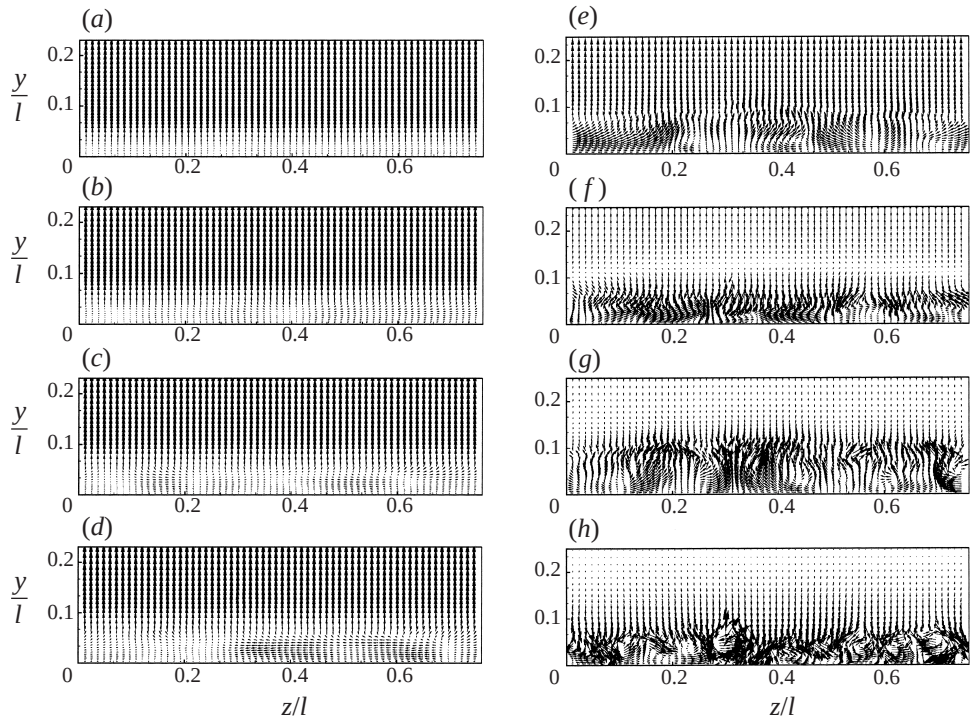

FIGURE 12. Instantaneous velocity vectors (w, v) in the (z, y)-plane at (*a*) $x/l = 0.1$, (*b*) 0.2, (*c*) 0.3, (*d*) 0.4, (*e*) 0.5, (*f*) 0.6, (*g*) 0.7, (*h*) 0.8.

dimensional motions can be seen in figure 12, showing velocity vectors on the (x, z)-plane at several streamwise locations $x/l = 0.1$, 0.2, 0.3, 0.4, 0.5, 0.6 and 0.8. At $x/l = 0.1$ the flow is still two-dimensional and the spanwise velocity is tiny. Three-dimensional motions are barely observable at $x/l = 0.2$ and develop slowly, as shown at $x/l = 0.3$ and $x/l = 0.4$. Noticeable three-dimensional motions appear at $x/l = 0.5$ and develop much more quickly afterwards; see the figures at $x/l = 0.6$, 0.7 and 0.8.

Figure 13 shows the three-dimensional contours of fluctuating pressure at three different times. It can be seen from figure 13(*a*) that two-dimensional vortical structures exist at the early stage of the bubble and then become distorted owing to three-dimensional motion setting in. Hairpin vortices form further downstream around or after the reattachment point, as shown in figures 13(*b*) and 13(*c*), and eventually break down to turbulence around or after the reattachment point. The spanwise distance between the ends of the hairpin vortices is about 0.31, which is roughly the same as the Kelvin–Helmholtz wavelength in the present study. This is worthy of note as it is shown by Roshko (1981) that the spanwise distance between the streamwise vortices in the transition region of an initially laminar mixing layer is approximately equal to the Kelvin–Helmholtzs spacing. Tafti & Vanka (1991) conclude from their numerical study of the unsteady separated flow over a blunt plate held normal to a uniform stream that the separation bubble is characterized by large coherent structures in the form of spanwise vortices. They are three-dimensional in nature with their approximate spanwise size between 20% to 30% of the mean reattachment length, similar to that observed in the present study.

The hairpin vertical structures identified in the present study also confirm the ideas

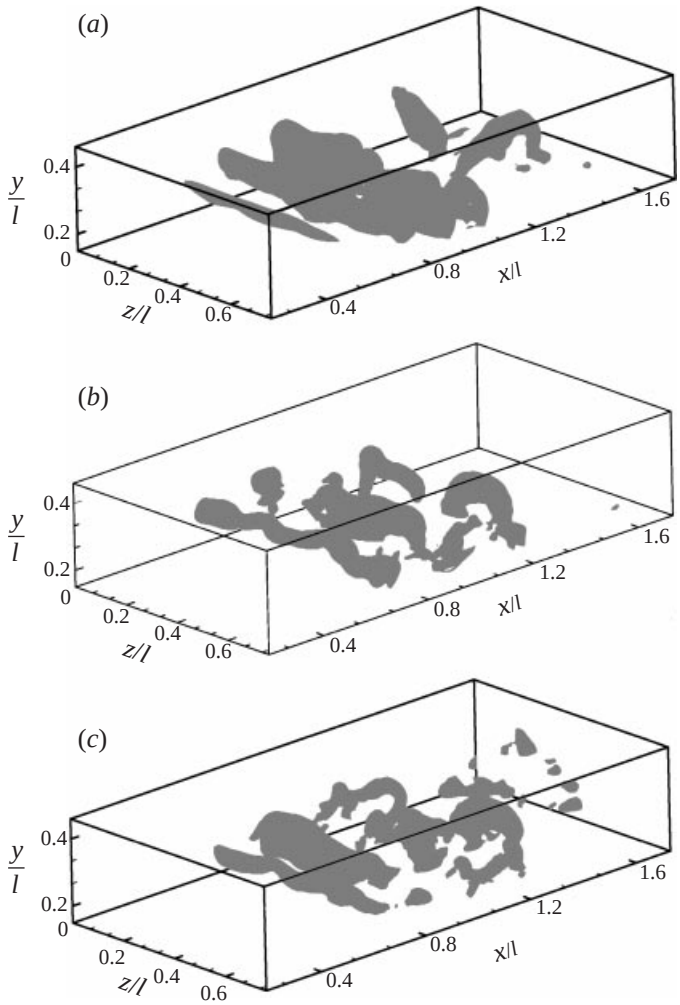

FIGURE 13. Contours of fluctuating pressure showing vortex cores at three times.

put forward by Kiya & Sasaki (1985) from their experimental study that hairpin vortices exist in the separated flow region. Large-scale structures exist not only in transitional separated flow but also in turbulent separated flow as reported by Na & Moin (1998) in their DNS of a separated turbulent boundary layer on a flat plate due to an adverse pressure gradient. Large-scale structures are clearly identified in the transition process associated with the separation bubble and go through several stages: two-dimensional, distorted three-dimensional, and hairpin vortices, a breakdown stage and eventually turbulence after the reattachment point in the present study.

3.2.6. *Boundary-layer development after reattachment*

It is noted that the boundary layer downstream of reattachment is initially quite different from an equilibrium turbulent boundary layer. It takes about seven bubble lengths for the log law to be re-established, as shown numerically by Alam & Sandham (1999) in their DNS study of a laminar separation bubble on a flat plate due to a adverse pressure gradient. Castro & Epik (1999) demonstrate experimentally in the boundary layer behind a separation bubble on a flat plate with a blunt

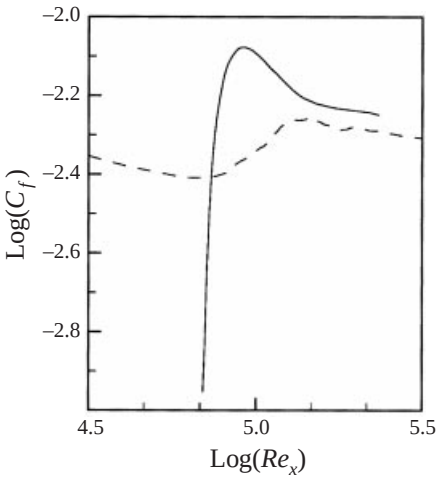

FIGURE 14. Friction coefficient. ——, current results after reattachment; – – –, bypass transition on a flat plate.

leading edge that an energetic outer layer is decaying slowly, preventing the inner layer from attaining its canonical form. In the inner region, although the log law is eventually re-established, the turbulence structure has not developed normally even by 70 boundary layer thicknesses downstream. This has been also observed in experiments and simulations of the backward-facing step flow (Bradshaw & Wong 1972; Le *et al.* 1997) indicating that many features of the developing boundary layer are qualitatively independent of the precise nature of the separation and reattachment process. The discussion in the present study will not focus on the re-establishment of the log law layer, as previous studies have clearly demonstrated this point, and also the computational box used in the present study is not long enough for the inner layer to develop into its canonical form. We consider that the entire transition process may involve a further significant stage of instability downstream of reattachment and will elucidate the boundary-layer development process just after reattachment. An earlier study (Voke & Yang 1999) indicated that the boundary-layer development immediately after the reattachment is reminiscent of that found in simulations of flat-plate boundary-layer bypass transition under free-stream turbulence (Voke & Yang 1995). In order to clarify this, a more detailed comparison with the bypass transition will be presented here.

Figure 14 shows the skin friction coefficient after the mean reattachment. (Re_x in the present study is based on the free-stream velocity and the distance from the blend point where the separation occurs). For comparison, the Re_x in the present case is shifted about 0.83 towards the higher value, to the location where the friction coefficient starts to increase in the bypass transition study (Voke & Yang 1995). The friction coefficient shoots up very rapidly (compared with the bypass transition case) to a higher value within a very short distance after reattachment, but then drops down relatively slowly to a level comparable with that of the turbulent boundary layer in the bypass transition case (though still higher) and may take much longer to recover and reach the same level, as discussed above. A similar picture is observed in figure 15, where the shape factor drops very quickly to a lower value. (Re_x in the present study is shifted about 0.83 again to the location where the shape factor starts to drop quickly in the bypass transition case.) Figure 16 shows the $\overline{u'^2}$ production

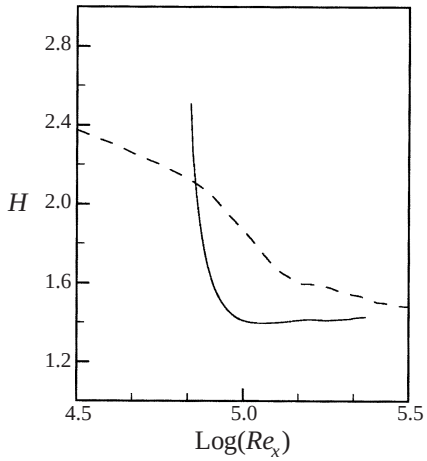

FIGURE 15. Shape factor. ——, current results after reattachment; – – –, bypass transition on a flat plate.

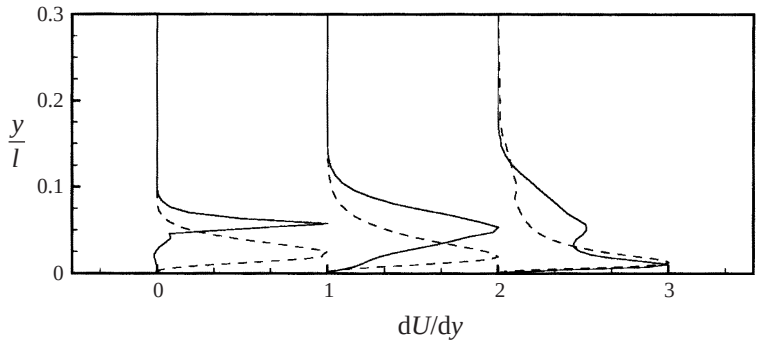

FIGURE 16. Normalized production term $u'v'\mathrm{d}U/\mathrm{d}y$. ——, current results at $x/l = 0.44$, 1.09, 1.64; – – –, bypass transition at $x = 45$, 95, 195 mm.

term $\overline{u'v'}\mathrm{d}U/\mathrm{d}y$ at the same three locations; in the bypass transition study this term plays an important role. As can be seen from figure 16, in the bypass transition case, turbulence production mainly occurs near the wall and the peak becomes closer to the wall from the disturbed laminar layer ($x = 45$ mm) through the transition region ($x = 95$ mm) to the turbulent boundary layer ($x = 195$ mm). In the present study, turbulence production in the bubble is concentrated in the free shear layer region and even just after the reattachment still mainly occurs in the outer layer. The wall shear layer starts to build and it can be seen that at $x/l = 1.64$ the near wall peak is well established. The peak in the outer layer is still visible at this location which confirms that the outer layer is indeed decaying slowly, as concluded by Castro & Epik (1999).

The fact that some form of turbulent boundary layer is established very rapidly, within a short distance after reattachment, is indicated by the skin friction coefficient and shape factor shown above. The layer will take much longer to attain its canonical form, i.e. for the log law layer and the inner layer turbulence structure to re-establish. The evidence is insufficient to support the scenario that it goes through a 'bypass transition stage' (Voke & Yang 1999) because the instantaneous flow around the mean reattachment point is highly unsteady and turbulent, though it may be dominated mainly by large-scale two- and three-dimensional vortical structures formed in the free

shear layer. These large-scale structures start to break down into small-scale structures at around the mean reattachment point and some form of turbulent boundary layer develops rapidly afterwards. It clearly takes some time for the small scale turbulence structure to develop in the inner layer, in interaction with the outer-layer structures.

4. Discussion and concluding remarks

The study of separated boundary-layer transition on a flat plate with a semicircular leading edge has been carried out numerically and the entire transition process leading to breakdown to turbulence has been elucidated and visualized using the LES data. From detailed analysis, it has been shown that the free shear layer formed in the separation bubble is inviscidly unstable via the Kelvin–Helmholtz instability mechanism, and the unsteadiness starts from about $x/l = 0.15$. These initial two-dimensional instability waves grow downstream linearly, with slow development of three-dimensional motions via a secondary instability mechanism responsive to any small spanwise disturbance. Further downstream the distorted spanwise two-dimensional vortices roll up, leading to streamwise vorticity formation, and nonlinear interaction starts once the fluctuation level reaches a threshold level. Significant three-dimensional motions develop much more rapidly at about $x/l = 0.5$, with u', v' and w' growing at a much higher rate compared with the early slow development stage and reaching maximum values just before the mean reattachment point (figure 6). Breakdown to turbulence occurs around the mean reattachment point and the flow develops into a turbulent boundary layer rapidly after the reattachment, though it takes much longer for the log law layer and the inner region turbulence structures to develop. Vortical structures (two-dimensional, three-dimensional hairpin vortices) have been identified at various stages of the transition process. A peak–valley spanwise wave structure is also found in the separation bubble.

Vortex shedding from the separated shear layer has been observed. This is not periodic in the sense that a unique frequency exists, and the instantaneous reattachment position moves over a distance up to 53% of the mean reattachment length. This large-scale movement, and especially the power spectrum at three streamwise positions, have shown that the characteristic shedding frequency varies in the range $\sim 0.35U_0/l$–$1.14U_0/l$ ($St = 0.0034$–0.011. The average frequency can be estimated at about $0.77U_0/l$ ($St = 0.0074$), while the measured dominant shedding frequency is about $0.65U_0/l$ (cf. Kiya & Sasaki 1983, 1985; Cherry *et al.* 1984). It is demonstrated in the present study that the so-called low-frequency flapping phenomenon ($0.125U_0/l$–$0.2U_0/l$) observed in several experimental studies of separated flow over a blunt plate (Kiya & Sasaki 1983, 1985; Cherry *et al.* 1984) may be associated with a larger shrinkage of the bubble caused by a 'big vortex shedding' which occurs at a lower frequency. In addition, the high selective frequency shedding ($4.2U_0/l$) reported numerically by Tafti & Vanka (1991) is not observed in the present study.

There are many different routes to transition depending on many factors. In the present study of a separated boundary layer, transition starts with Kelvin–Helmholtz instability; three-dimensional motions develop initially at a slow rate associated with peak–valley wave structures via a secondary instability process, until about $x/l = 0.5$, where nonlinear interactions take a central role and significant three-dimensional motions start to develop. The breakdown stage is characterized by the irregular shedding of large-scale vortices associated with free shear-layer roll-up and, hence, the formation of hairpin vortices. Large vortical structures travel downstream and impinge on the wall, where a turbulent boundary layer forms rapidly, but it takes

quite a long distance downstream (certainly beyond the current computational box) for the log law and inner turbulence structures to develop as reported by many studies.

The authors gratefully acknowledge the support of EPSRC, DERA and Rolls–Royce plc who funded this research. We thank Dr Mark Savill and Dr John Coupland for their advice. Thanks are also due to Dr Robert Bowles and Professor Frank Smith for valuable suggestions and discussions. The computations were carried out on a Cray J932 at Rutherford-Appleton Laboratory, funded by EPSRC.

REFERENCES

Alam, M. & Sandham, N. D. 1999 Direct numerical simulation of 'short' laminar separation bubbles with turbulent reattachment. *J. Fluid Mech.* **403**, 223–250.

Armenio, V., Piomelli, U. & Fioretto, V. 1999 Application of a Lagrangian mixed subgrid-scale model in generalized coordinates. In *Direct and Large-Eddy Simulation III* (ed. P. R. Voke, N. Sandham & L. Kleiser), pp. 135–146. Kluwer.

Bradshaw, P. & Wong, F. Y. F. 1972 The reattachment and relaxation of a turbulent shear layer. *J. Fluid Mech.* **52**, 113–135.

Castro, I. & Epik, E. 1999 Boundary layer development after a separated region. *J. Fluid Mech.* **374**, 91–116.

Chandrasekhar, S. 1961 *Hydrodynamic and Hydromagnetic Stability*. Clarendon.

Cherry, N. J., Hillier, R. & Latour, M. P. 1984 Unsteady measurements in a separated and reattaching flow. *J. Fluid Mech.* **144**, 13–46.

Craik, A. D. D. 1982 *Wave Interaction and Fluid Flows*. Cambridge University Press.

Danaila, I., Dusek, J. & Anselmet, F. 1997 Direct numerical simulation of the free, unsteady, round, unforced jet at low Reynolds numbers. In *Direct and Large-Eddy Simulation II* (ed. J. Chollet, P. R. Voke & L. Kleiser), pp. 1–10. Kluwer.

Deardorff, J. W. 1970 A numerical study of three-dimensional turbulent channel flow at large Reynolds number. *J. Fluid Mech.* **41**, 452–480.

Dovgal, A. V., Kozlov, V. V. & Michalke, A. 1994 Laminar boundary layer separation: instability and associated phenomena. *Prog. Aerospace Sci.* **30**, 61–94.

Eaton, J. K. & Johnston, J. P. 1981 A review on subsonic turbulent flow reattachment. *AIAA J.* **19**, 1093–1100.

Eaton, J. K. & Johnston, J. P. 1982 Low frequency unsteadiness of a reattaching turbulent shear layer. In *Turbulent Shear Flows 3* (ed. L. J. S. Bradbury, F. Durst, B. F. Launder, F. W. Schmidt & J. H. Whitelaw), pp. 162–170. Springer.

Gartshore, I. P. & Savill, M. 1982 Some effects of free stream turbulence on the flow around bluff bodies. *Euromech 160: Periodic Flow and Wake Phenomena*, Berlin.

Gaster, M. 1963 On stability of parallel flows and the behaviour of separation bubbles. PhD thesis, University of London.

Germano, M., Piomelli, U., Moin, P. & Cabot, W. H. 1991 A dynamic subgrid-scale eddy viscosity model. *Phys. Fluids* A **3**, 1760–1765.

Ghosal, S., Lund, T. S., Moin, P. & Akselvoll, K. 1995 A dynamic localization model for large-eddy simulation of turbulent flow. *J. Fluid Mech.* **286**, 229–255.

Hillier, R. & Cherry, H. J. 1981*a* Pressure fluctuations under a turbulent shear layer. In *Proc. 3rd Turbulent Shear Flow Symp.* University of California, Davis, pp. 23–29.

Hillier, R. & Cherry, H. J. 1981*b* The effects of stream turbulence on separation bubbles. *J. Wind Engng Indust. Aero.* **8**, 49–58.

Ho, C. M. & Huerre, P. 1984 Perturbed free shear layers. *Ann. Rev. Fluid Mech.* **16**, 365–424.

Jordan, S. A. 1999 A large-eddy simulation methodology in generalized curvilinear coordinates. *J. Comput. Phys.* **148**, 322–340.

Kaltenbach, H. J. & Choi, H. 1995 Large-eddy simulation of flow around an airfoil on a structured mesh. *Annual Research Briefs 1995*, Center for Turbulence Research, Stanford University and NASA Ames, pp. 51–60.

Kiya, M. & Sasaki, K. 1983 Structure of a turbulent separation bubble. *J. Fluid Mech.* **137**, 83–113.

Kiya, M. & Sasaki, K. 1985 Structure of large-scale vortices and unsteady reverse flow in the reattaching zone of a turbulent separation bubble. *J. Fluid Mech.* **154**, 463–491.

Kiya, M., Sasaki, K. & Arte, M. 1982 Discrete-vortex simulation of a turbulent separation bubble. *J. Fluid Mech.* **120**, 219–244.

Le, H., Moin, P. & Kim, J. 1997 Direct numerical simulation of turbulent flow over a backward-facing step. *J. Fluid Mech.* **330**, 349–374.

Lilly, D. K. 1966 On the application of the eddy viscosity concept in the inertial sub-range of turbulence. *NCAR manuscript* **123**, NCAR, Boulder, CO.

Lilly, D. K. 1992 A proposed modification of the Germano subgrid scale closure method. *Phys. Fluids* A **4**, 633–635.

Lin, J. C. M. & Pauley, L. L. 1993*a* Unsteady laminar separation on low-Reynolds number airfoils. *AIAA paper* 93-0209.

Lin, J. C. M. & Pauley, L. L. 1993*b* Unsteady view of transitional separation bubbles. *Separated Flow Symp. ASME Fluids Engng Conf.*

Monkewitz, P. A. & Huerre, P. 1982 The influence of the velocity ratio on the spatial instability of mixing layers. *Phys. Fluids* **25**, 1137–1143.

Na, Y. & Moin, P. 1998 Direct numerical simulation of a separated turbulent boundary layer. *J. Fluid Mech.* **374**, 379–405.

Niew, T. R. 1993 The stability of the flow in a laminar separation bubble. PhD thesis, University of Cambridge.

Ota, T. & Itasaka, M. 1976 A separated and reattached flow over a blunt flat plate. *Trans. ASME* I: *J. Fluid Engng* **98**, 79–86.

Ota, T. & Narita, M. 1978 Turbulence measurements in a separated and reattached flow over a blunt flat plate. *Trans. ASME* I: *J. Fluid Engng* **100**, 224–228.

Pauley, L. L., Moin, P. & Reynolds, W. C. 1990 The structure of two-dimensional separation. *J. Fluid Mech.* **220**, 397–411.

Rayleigh, Lord 1880 *Scientific Papers*, vol. 1, pp. 474–487. Cambridge University Press.

Ripley, M. D. & Pauley, L. L. 1993 The unsteady structure of two-dimensional separation bubble. *Phys. Fluids* A **5** (12), 3099–3106.

Rist, U., Maucher, U. & Wagner, S. 1996 Direct numerical simulation of some fundamental problems related to transition in laminar separation bubbles. In *Proc. Comput. Fluid Dyn. Conf. ECCOMAS 96*, pp. 319–325.

Roshko, A. 1981 The plane mixing layerflow visualization results and three-dimensional effects. In *The Role of Coherent Structures in Modelling Turbulence and Mixing* (ed. J. Jimenez). Lecture Notes in Physics, vol. 136, pp. 208–217. Springer.

Schlichting, H. 1968 Boundary-Layer Theory, 6th edn. McGraw-Hill.

Schumann, U. 1973 Results of a numerical simulation of turbulent channel flows. In *Intl Meeting on Reactor Heat Transfer* (ed. M. Dalle-Donne), pp. 230–251.

Schumann, U. 1975 Subgrid scale modelling for finite difference simulations of turbulent flows in plane channels and annuli. *J. Comput. Phys.* **18**, 376–404.

Smagorinsky, J. 1963 General circulation experiments with the primitive equations. I. The basic experiment. *Mon. Weather Rev.* **91**, 99–164.

Spalart, P. R. & Strelets, M. Kh. 2000 Mechanisms of transition and heat transfer in a separation bubble. *J. Fluid Mech.* **403**, 329–349.

Tafti, D. K. & Vanka, S. P. 1991 A three-dimensional study of flow separation and reattachment on a blunt plate. *Phys. Fluids* A **3**, 2887–2909.

Tollmien, W. 1935 Ein allgemeines kriterium der instabilitat laminarer geschwindigkeits veteilungen. *Nachr. Ges. Wiss. Gottingen, Math. Phys. Klasse, Fachgruppe I*, **1**, 79–114.

Urbin, G. & Metais, O. 1997 Large-eddy simulation of three-dimensional spatially-developing round jets. *Direct and Large-Eddy Simulation II* (ed. J. Chollet, P. R. Voke & L. Kleiser), pp. 35–46.

Voke, P. R. & Yang, Z. Y. 1995 Numerical study of bypass transition. *Phys. Fluids* **7**, 2256–2264.

Voke, P. R. & Yang, Z. Y. 1998 Efficient methods for LES of aerofoil and turbine blade flows. *Numerical Methods for Fluid Dynamics VI* (ed. M. J. Baines), pp. 137–148, ICFD.

Voke, P. R. & Yang, Z. Y. 1999 Large-eddy simulation of separation and transition for turbomachinery flows. *Industrial and Environmental Applications of Direct and Large-Eddy Simulation* (ed. S. Biringen, H. Ors, A. Tezel & J. H. Ferziger), pp. 46–63. Springer.

VOKE, P. R., YANG, Z. Y. & SAVILL, A . M. 1996 Large-eddy simulation of transition following a leading-edge separation bubble. In *Engineering Turbulence Modelling Experiments*, vol. 3 (ed. W. Rodi & G. Bergeles), pp. 601–610. Elsevier.

WILSON, P. G. & PAULEY, L. L. 1995 Two-dimensional large eddy simulation of a separation bubble. *Symp. Separated and Complex Flows ASME/JSME Fluids Engng Conf.*